Nano Research
2019, 12(8): 1871–1879

ISSN 1998-0124 CN 11-5974/O4
https://doi.org/10.1007/s12274-019-2450-4

Research Article

Explaining the influence of dopant concentration and excitation power density on the luminescence and brightness of β-$NaYF_4$:Yb^{3+},Er^{3+} nanoparticles: Measurements and simulations

Martin Kaiser[1], Christian Würth[1], Marco Kraft[1], Tero Soukka[2], and Ute Resch-Genger[1] (✉)

[1] *Division Biophotonics, Federal Institute for Materials Research and Testing (BAM), Richard-Willstaetter-Str. 11, D-12489 Berlin, Germany*
[2] *Department of Biotechnology, University of Turku, Kiinamyllynkatu 10, Turku, FI-20520, Finland*

Received: 17 February 2019 / **Revised:** 29 May 2019 / **Accepted:** 30 May 2019

ABSTRACT

We assessed the influence of Yb^{3+} and Er^{3+} dopant concentration on the relative spectral distribution, quantum yield (Φ_{UC}), and decay kinetics of the upconversion luminescence (UCL) and particle brightness (B_{UC}) for similarly sized (33 nm) oleate-capped β-$NaYF_4$:Yb^{3+},Er^{3+} upconversion (UC) nanoparticles (UCNPs) in toluene at broadly varied excitation power densities (P). This included an Yb^{3+} series where the Yb^{3+} concentration was varied between 11%–21% for a constant Er^{3+} concentration of 3%, and an Er^{3+} series, where the Er^{3+} concentration was varied between 1%–4% for a constant Yb^{3+} concentration of 14%. The results were fitted with a coupled rate equation model utilizing the UCL data and decay kinetics of the green and red Er^{3+} emission and the Yb^{3+} luminescence at 980 nm. An increasing Yb^{3+} concentration favors a pronounced triphotonic population of $^4F_{9/2}$ at high P by an enhanced back energy transfer (BET) from the $^4G_{11/2}$ level. Simultaneously, the Yb^{3+}-controlled UCNPs absorption cross section overcompensates for the reduction in Φ_{UC} with increasing Yb^{3+} concentration at high P, resulting in an increase in B_{UC}. Additionally, our results show that an increase in Yb^{3+} and a decrease in Er^{3+} concentration enhance the color tuning range by P. These findings will pave the road to a deeper understanding of the energy transfer processes and their contribution to efficient UCL, as well as still debated trends in green-to-red intensity ratios of UCNPs at different P.

KEYWORDS

upconversion, quantum yield, color tuning, nanoparticles, dopant concentration, rate equation model

1 Introduction

Lanthanide-based upconversion nanoparticles (UCNPs) with their unique ability to convert two or more near infrared (NIR) to higher energy photons have been increasingly used in bioimaging, sensing, photovoltaics, thermometry, and anticounterfeiting [1–8]. This also initiated many studies on the photophysics of these materials, which are governed by a multitude of interacting energy levels, often with the aim of rationally designing UCNPs with maximum brightness and control of their upconversion luminescence (UCL) for specific applications. Parameters assessed included size and spatial arrangement of the sensitizer and activator ions in increasingly sophisticated core-shell nanostructures, as well as the exploitation of plasmonic interactions or dye sensitization [3, 4, 9–12]. One of the most studied UCNPs converters is β-$NaYF_4$:Yb^{3+},Er^{3+} UCNPs excitable at 976 nm. The optimum dopant concentration of β-$NaYF_4$:Yb^{3+},Er^{3+} is typically assumed to be 17%–20% of the sensitizer Yb^{3+} and 2%–3% of the activator Er^{3+} [8, 13]. Nevertheless, a comprehensive study of the dependence of the Er^{3+} green-to-red emission ratio (I_{green}/I_{red}), the UC quantum yield (Φ_{UC}), and the brightness (B_{UC}) on the concentration of the active lanthanide ions for a broad P-range is still missing. Also, the long-term debates of the UC processes activating the red emission have only recently been settled (see Fig. 1) [9, 14–31]. It is well known that an increase of Yb^{3+} enhances the red emission at cost of the green emission band [18–20, 32–35]. An increasing Er^{3+} concentration should also favor a red emission via the increased nonradiative relaxation from the $^2H_{11/2}$,$^4S_{3/2}$ level or cross relaxation (CR) processes between Er^{3+} ions. However, different and sometimes even opposite trends of I_{green}/I_{red} have been reported in the literature [32, 33, 36–38]. A comparison of material performance is, however, further complicated by the fact that the Er^{3+} concentration dependent I_{green}/I_{red} is also affected by excitation power density (P), yet literature data is typically provided only for a single P value. Consequently, up to now no comprehensive rate equation analysis has been performed that describes the mechanism(s) responsible for the Yb^{3+} and Er^{3+} concentration effects. Figure 1 summarizes the population pathways of the green and red emissive Er^{3+} levels derived for $NaYF_4$:Yb^{3+},Er^{3+} particles of different size and particle architecture (core-only; core-shell) in less and more quenching environments and different P regimes. The biphotonically populated green Er^{3+} 520/540 nm ($^2H_{11/2}$/$^4S_{3/2}$ → $^4I_{15/2}$) emission is fed by energy transfer (ET) from two excited Yb^{3+} ions. The red Er^{3+} ($^4F_{9/2}$ → $^4I_{15/2}$) emission at 655 nm, however, can be populated via two different biphotonic and triphotonic pathways. The exact nature of its activation depends on the material (size, crystal phase, bare or core-shell UCNPs), environment, and P. A constant value of I_{green}/I_{red} in the low P regime is indicative for the population of $^4F_{9/2}$ via $^2H_{11/2}$/$^4S_{3/2}$ (see Fig. 1(b)), which was shown e.g., by us for 25 nm-sized UCNPs in the solid state and dispersed in toluene [17]. Effective feeding of $^4F_{9/2}$ from $^4I_{13/2}$ after non-resonant (energy mismatch of about 1,000 cm^{-1}) Yb^{3+}-Er^{3+} ET (see Fig. 1(c)) requires a high population density of $^4I_{13/2}$. This can occur at low P for strongly quenched systems

Address correspondence to ute.resch@bam.de

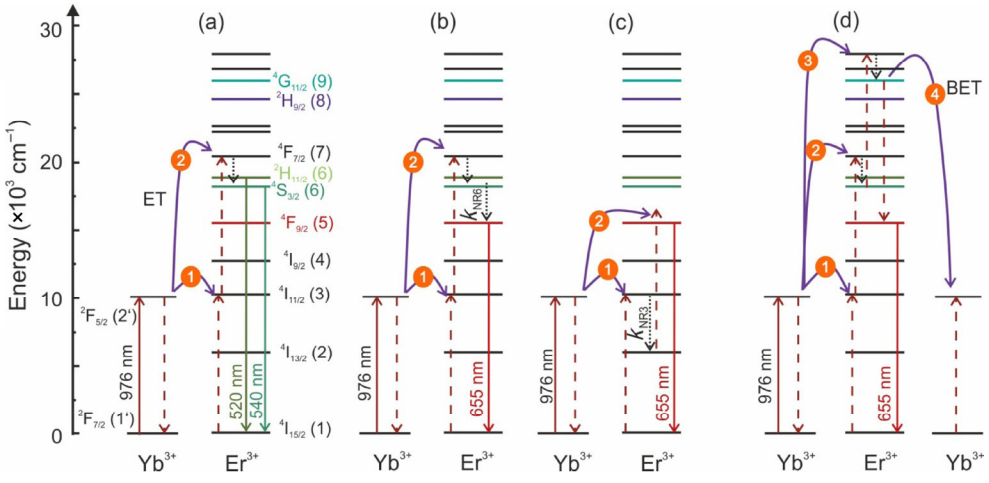

Figure 1 Energy level diagram summarizing the biphotonic population pathways of (a) the Er^{3+} 520/540 nm ($^2H_{11/2}/^4S_{3/2} \rightarrow {}^4I_{15/2}$) emission band and (b)–(e) different biphotonic and triphotonic population pathways of the red Er^{3+} ($^4F_{9/2} \rightarrow {}^4I_{15/2}$) energy level for different conditions. This includes (b) moderately quenched UCNPs, (c) strongly quenched UCNPs, and (d) systems with strongly diminished quenching, respectively, referring to different particle sizes, environments, and *P* ranges. For example, condition (b) is valid for core-only UCNPs with sizes of about 10–100 nm in an organic solvent at low *P* and condition (c) for ultra-small core-only UCNPs with sizes < 10 nm and for core-only UCNPs in water with sizes < 40 nm at low *P*. Condition (d) is valid for micrometer-sized upconversion particles at low and high *P*, core-only UCNPs in apolar and aqueous environments at very high *P*, and core-shell UCNPs with tight shells and very little core-shell intermixing, respectively. Solid lines present radiative transitions and dashed lines non-radiative transitions, respectively. The size regimes are estimated for β-$NaYF_4$:Yb^{3+},Er^{3+} excitable at 976 nm with dopant concentrations of Yb^{3+} of 17%–21% and Er^{3+} of 2%–3% from the literature data described in the text.

revealing high multi-phonon relaxation rates from the upper Er^{3+} level $^4I_{11/2}$ (see Fig. 1(c)). An indication of this population pathway via the $^4I_{13/2}$ energy level is increasing I_{green}/I_{red} values in the low *P* regime, as recently shown by us for UCNPs with sizes < 40 nm in water [16, 39]. For larger "less quenched" particles, the red emissive Er^{3+} $^4F_{9/2}$ energy level is typically populated by a triphotonic pathway via back energy transfer (BET) from the $^4G_{11/2}$ energy level of Er^{3+} to the $^2F_{7/2}$ energy level of Yb^{3+} (see Fig. 1(d)), as reported by the Berry group for a μm-sized powder and 90 nm-sized UCNPs dispersed in toluene [14, 15]. Berry et al. also suggested an alternative triphotonic activation pathway for the red emissive $^4F_{9/2}$ for "less quenched systems". This involved cross relaxation (CR) from the green $^2H_{11/2}$,$^4S_{3/2}$ to $^4I_{13/2}$ followed by ET to $^4F_{9/2}$ energy level [15]. A prerequisite for this process is a high population density of the $^4I_{13/2}$ level as is encountered for high Er^{3+} concentrations, favoring high CR rates, and under continuous wave excitation with high *P*. Our previous studies of UCNPs with sizes > 20 nm in organic solvents revealed the population of $^4F_{9/2}$ by a mixture of bi- and triphotonic channels at high *P* [16, 17, 39]. For none or less quenched core-shell UCNPs, the triphotonic activation of $^4F_{9/2}$ seems to be dominant [40–42], although core-shell intermixing can affect and even hamper the triphotonic activation of the red level as recently shown for ultra-small core-shell $NaGdF_4$:Yb^{3+},Er^{3+}@$NaYF_4$ particles with a core diameter of 3.7 nm and differently thick $NaYF_4$ passivation shells [43].

Aiming for a systematic study of these dopant concentration effects, we rationally designed two series of oleate-capped monodisperse core-only UCNPs of similar size (33.5 ± 0.5 nm, see Appendix A, Fig. S1 and Table S1 in the the Electronic Supplementary Material (ESM)) and surface chemistry, one Yb^{3+} series (Yb^{3+} concentration of 11%–21%; constant Er^{3+} amount of 3%) and one Er^{3+} series (Er^{3+} concentration of 1%–4%, constant Yb^{3+} amount of 14%). Thereby, the parameters known to affect UCL like particle size [17, 44] and environment [16, 45], as well as thickness and tightness of the shielding surface passivation shell [40] and core-shell intermixing [43, 46, 47] were excluded. Only the average distances between the Yb^{3+} and Er^{3+} ions were varied. Subsequently, the *P*-dependent UCL spectra, Φ_{UC} values, as well as the slope factor $n(P)$ of the green and red emission bands of Er^{3+} of both concentration series were studied in toluene. The experimental data were fitted with a coupled rate equation model taken from the Berry group [14], which involves nine Er^{3+} energy levels.

2 Results and discussion

2.1 Dopant-dependent UCL spectra and (de)population processes

First, we determined the *P*-dependent UCL spectra, relative spectral emission intensities ($I_{rel,\Delta\lambda}(P)$), and slope factors ($n(P)$) of the green Er^{3+} 520/540 nm ($^2H_{11/2}/^4S_{3/2} \rightarrow {}^4I_{15/2}$) and red Er^{3+} 655 nm ($^4F_{9/2} \rightarrow {}^4I_{15/2}$) emission bands of the 33 nm-sized oleate-capped UCNPs dispersed in toluene for the Yb^{3+} and Er^{3+} series (see Figs. 2 and 4). The $I_{rel,\Delta\lambda}(P)$ values (with $\Delta\lambda$ presenting either the center wavelength or color of the respective emission band) provide the contribution of each UC emission band to the overall UCL intensity in the wavelength region of 370–900 nm, and hence information on the relative population of the respective UC energy level. The *P*-dependent slope factor ($n(P)$) (see Eq. (1)) reveals the photonic order of the UC process of the respective emission band at low *P* far from saturation. $n(P)$ can be determined from the slope of a plot of the emission intensity as function of *P* on a double logarithmic scale (see Fig. S2 in the ESM). We also produced a rough estimate of the contribution of biphotonic and triphotonic processes to the population of the red $^4F_{9/2}$ energy level of Er^{3+} from the $n(P)$ values derived for the red, green, and purple Er^{3+} emission bands ($n_{red}(P)$, $n_{green}(P)$ and $n_{purple}(P)$), see Appendix B in the ESM. As the *P*-dependent depopulation mechanisms of $^4F_{9/2}$ become important at high *P*, this attempt provides only a lower and upper limit for the biphotonic and triphotonic population contributions (see Fig. S2 in the ESM).

Subsequently, the UCL spectra were measured in a *P* range from P_{unsat} = 1.8 W·cm^{-2} to P_{sat} = 380 W·cm^{-2}, where $n_{green}(P)$ changes from two to one for the investigated UCNPs using a previously described integrating sphere setup [17]. This change reflects the competing of depopulation and population processes of the Er^{3+} levels with increasing *P*, which is here referred to as saturation behavior of the UC process. As a criterion for the onset of saturation, we use $n_{green}(P)$ = 1.9. The values of P_{unsat} and P_{sat} are then employed as corner stones for the comparison of the UCL features of our UCNPs.

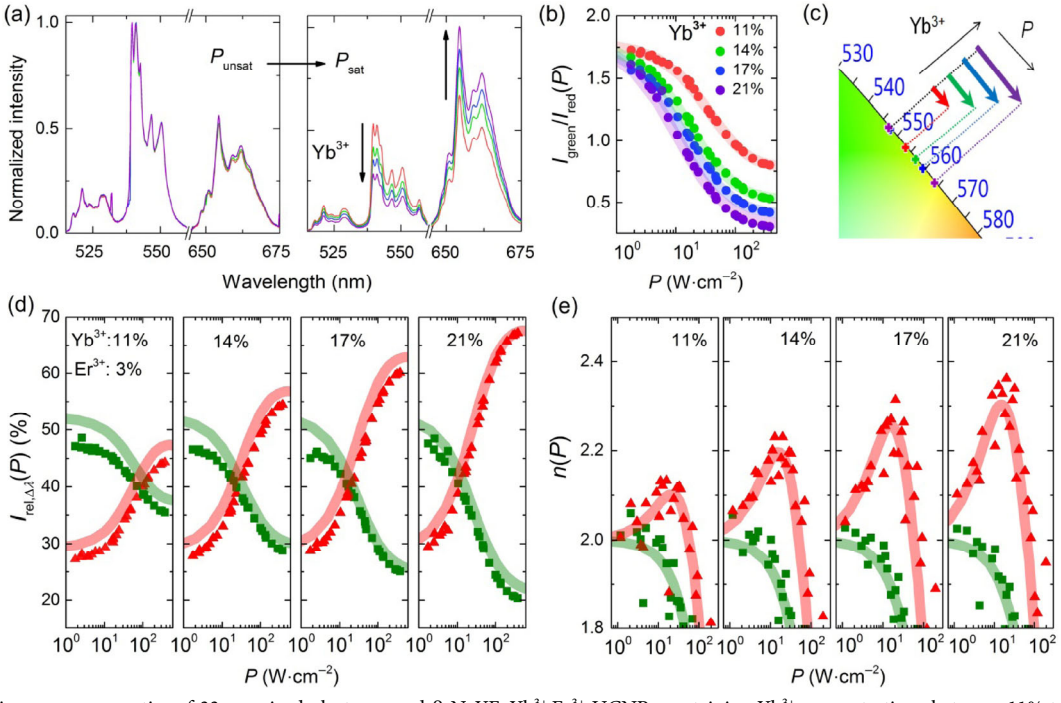

Figure 2 Photoluminescence properties of 33 nm-sized oleate-capped β-$NaYF_4$:Yb^{3+},Er^{3+} UCNPs containing Yb^{3+} concentrations between 11% to 21% and a constant Er^{3+} concentration of 3% dispersed in toluene. (a) UCL spectra shown from 515 to 675 nm obtained at P_{unsat} of 1.8 W·cm^{-2} and P_{sat} of 380 W·cm^{-2}, respectively. All spectra were normalized by division by the total UCL intensity integrated from 370 to 900 nm. (b) *P*-dependent I_{green}/I_{red} values. (c) CIE diagram visualizing the color tuning range by varying *P*. (d) *P*-dependent relative contribution $I_{rel,\Delta\lambda}(P)$ of the green and red Er^{3+} emission bands to overall UCL. The apparent offset between the measured and simulated $I_{rel,\Delta\lambda}(P)$ values is ascribed to the neglected contribution of the $^4I_{9/2}$ level (from which the 810 nm emission band originates). (e) $n(P)$ values of the green and red Er^{3+} emission. The experimental data are always given as symbols and the results from the simulation of the corresponding parameters or properties using coupled rate equations are provided as lines.

The interpretation of the influence of the dopant concentration on ET, BET, and the nonradiative deactivation rates (k_{NR}) was supported by a model of coupled rate equations adapted from the Berry group [14, 41], utilizing the *P*-dependent UCL spectra and luminescence decay kinetics (Fig. 3). In contrast to the Berry group, who simulated core-only particles with a dark layer, i.e., a highly quenched outer layer [41], we chose to use average rate constants covering the whole particle volume. Also, we simplified the rate equation analysis by neglecting the contribution of the 810 nm emission to overall UC intensity (< 10%; see Fig. S3 in the ESM) and changes in CR and Er^{3+}-Er^{3+} ET rate constants (k_{CR4}, k_{CR6}, k_{UC2}; see Fig. S4 in the ESM). Loop processes were reduced by setting k_{NR} of the red and the 810 nm energy levels to 0 and 100 s^{-1}, respectively. Additionally, we set the value of k_{NR} of the Er^{3+} 980 nm level (k_{NR3}) to 1,000 s^{-1} compared to about 100,000 s^{-1} employed by Berry 2017 for (24 × 56) nm sized $NaYF_4$:Yb^{3+}(17%),Er^{3+}(3%) [41]. These simplifications have to be considered when evaluating and comparing the obtained rate constants (see Table S2 in the ESM). In the first step, the *P*-dependent UCL behavior of the UCNPs containing 14% Yb^{3+} and 3% Er^{3+} was fitted, since this sample is part of both dopant concentration series. The fitting procedure steps and the set of rate constants varied are detailed. (Appendix C and Tables S2 in the ESM). Secondly, the influence of the dopant concentration was considered by tuning as few parameters as possible (see Tables S3 and S4, and Fig. S5 in the ESM). This was achieved by introducing new parameters as scaling factors to adapt ET and BET to changes of dopant ion distances determined by the respective dopant concentrations (see Eq. (S5) in the ESM). For the Yb^{3+} series, we varied three and for the Er^{3+} concentration series four parameters, including the respective dopant concentration level, described in the following subsections. The nonradiative deactivation of the excited active lanthanide ions at the UCNPs surface was considered by a reduction of the Yb^{3+}-Er^{3+} ET rate (k_{ET1-3}) reported in 2014 [14] by a factor of 100. For the Yb^{3+}-Er^{3+} ET rate constant k_{ET5-8} depopulating the red Er^{3+} level to the purple level we obtained a value of 1.56 × 10^{-15} cm^3·s^{-1}. This value closely matches the value of 1.76 × 10^{-15} cm^3·s^{-1} reported by the Berry group in 2014 [14]. In their new report in 2017, they revised the k_{ET5-8} value and set it to zero [41]. This assumption did not provide satisfying fits for our experimental data.

2.1.1 *Yb^{3+} concentration series*

Figure 2(a) shows the green and red UCL bands of Er^{3+} of the Yb^{3+} series at P_{unsat} = 1.8 W·cm^{-2} in the unsaturated regime and at P_{sat} = 380 W·cm^{-2} ($\Phi_{UC}(P_{sat}) = \Phi_{UC,max}$). This data is normalized to the overall UCL integrated from 370 to 900 nm. For each sample, I_{green} is about two-fold higher than I_{red} at P_{unsat}. The fact that the UCL spectra at P_{unsat} are independent of Yb^{3+} concentration suggests comparable rate constants of the UC process. This supports the high quality and close size match of our UCNPs, as particularly the I_{green}/I_{red} is known to be sensitive to parameters like size, distribution of dopant ions in the particle volume, surface properties, and defect densities [16, 17, 43–47]. On contrary, for P_{sat}, $I_{rel,red}(P)$ is enhanced by increasing the Yb^{3+} concentration, leading to a diminution of the $I_{green}/I_{red}(P_{sat})$ values from 0.8 to 0.3 for Yb^{3+} concentrations of 11% and 21% (Fig. 1(b)). This is also reflected by the chromaticity or CIE (CIE: International Commission of Illumination) diagram in the CIE 2015 10° *x*,*y* color space shown in Fig. 2(c), providing normalized colors of appearance to the human eye. This figure reveals that the perceived colors can be modulated by *P*. UCNPs doped with 21% Yb^{3+} show the highest tuning range in the color space, covering a wavelength region of 547 to 564 nm that exceeds the width of the tunable spectral range of UCNPs doped with 11% Yb^{3+} by a factor of about four. Higher Yb^{3+} concentrations than the dopant concentrations used by us are expected to provide an even higher color space tuning range extending further into the red spectral region. The experimentally determined $I_{rel,green}(P)$ and $I_{rel,red}(P)$ values of the Yb^{3+} series are summarized in Fig. 2(d). For P_{unsat} $I_{rel,green}$ and $I_{rel,red}$ are independent of Yb^{3+} concentration with values

of 47% and 28%, respectively. On contrary, for to P_{sat}, $I_{rel,red}$ increases from 44% to 67% and $I_{rel,green}$ decreases from 35% to 20% for UCNPs with Yb^{3+} concentrations increasing from 11% to 21%. As a result of the enhanced $I_{rel,red}(P_{sat})$, also the P values, where $I_{rel,green}(P)$ and $I_{rel,red}(P)$ cross, termed here P_{cross}, decrease from about 80 W·cm^{-2} to about 20 W·cm^{-2} for our UCNPs with Yb^{3+} concentrations of 11% and 21%, respectively. This indicates that P_{cross}, which was recently suggested by us as a simple measure for UC efficiency [42], can be exploited for this purpose only for materials with comparable Yb^{3+} dopant concentration. As shown in Fig. 2(e), for P_{unsat} both the green and the red emission clearly show a biphotonic behavior. This is indicated by $n_{green}(P_{unsat})$ and $n_{red}(P_{unsat})$ values of two. For all samples of the Yb^{3+} series, the shape of $n_{green}(P)$, reflecting the saturation behavior of the UC process, is identical, although an increase in the number of Yb^{3+} ions populating the Er^{3+} 520/540 nm ($^2H_{11/2}/^4S_{3/2} \rightarrow {}^4I_{15/2}$) levels should shift $n_{green}(P)$ to lower P values. Our rate equation analysis reveals that these changes of the saturation behavior are compensated by an enhanced deactivation of the excited Yb^{3+} ions at the surface. This is supported by a shortening of the Yb^{3+} lifetime (see Fig. 3). The triphotonic activation of the red emission follows directly from $n_{red}(P)$ exceeding 2 for increasing P with a P threshold of about 5 W·cm^{-2}. The maximum value of $n_{red}(P)$, which varies between 2.1 and 2.3 for the samples studied, increases with increasing Yb^{3+} concentration. This indicates an increase of the triphotonic activation processes (see Fig. 1).

Subsequently, the experimentally derived values for $I_{rel,\Delta\lambda}(P)$, $n(P)$, and I_{green}/I_{red} were modeled. As previously described for the Yb^{3+} concentration series we modified: i) the density of the Yb^{3+} ions per cm^3, ii) a common scaling factor for the five ET and four BET rates, and iii) k_{NR} of the $^2F_{5/2}$ level of Yb^{3+} (k_{Yb_NR}). The results are shown as lines in Figs. 2(b), 2(d), 2(e), and 3(a).

The variation in the Yb^{3+} concentration between 11% to 21% induces changes in the average Yb^{3+}-Yb^{3+} distances from 8.8 to 7.1 Å. This distance equals about the average Er^{3+}-Yb^{3+} distance for these relatively low Er^{3+} concentrations as tested with a distance simulation. Our simulation reveals that all BET and ET rates increase by about 220% for this reduction in the average distance between the Yb^{3+} and Er^{3+} ions of 20% (see Table S3 and Fig. S5 in the ESM). These calculations also confirm that the Yb^{3+}-induced enhanced triphotonic population of the red $^4F_{9/2}$ Er^{3+} level from $^4G_{11/2}$ is related to enhanced

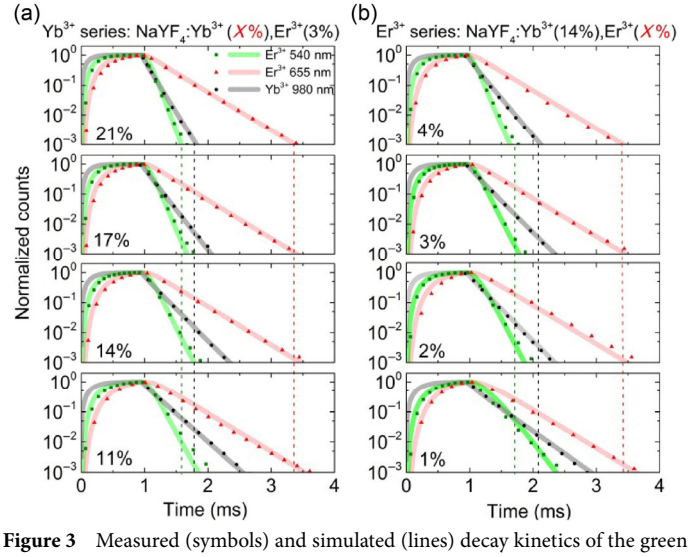

Figure 3 Measured (symbols) and simulated (lines) decay kinetics of the green (green) and red (red) Er^{3+} and the 980 nm Yb^{3+} (black) emission of 33 nm-sized oleate-capped β-$NaYF_4$:Yb^{3+}, Er^{3+} UCNPs dispersed in toluene. (a) Yb^{3+} series with the Yb^{3+} concentration being varied between 11% and 21% at a constant Er^{3+} concentration of 3%. (b) Er^{3+} series with the Er^{3+} concentration varying between 1% and 4% at a constant Yb^{3+} concentration of 14%. The measured data points were averaged using the data shown in Fig. S6 in the ESM.

BET rates (see Fig. 1(d)). However, at low P and hence, at relatively low population densities of the Er^{3+} levels, the BET rates have only a small influence as reflected by the observed Yb^{3+} concentration-independent UCL spectra. Subsequently, we experimentally determined the decay kinetics of the 980 nm Yb^{3+} and the green and red Er^{3+} emission and hence the lifetimes of the respective emissive states (see Fig. 3). This enables us to consider changes in k_{NR} of the $^2F_{5/2}$ level of Yb^{3+} (k_{Yb_NR}).

From the reduction of the Yb^{3+} lifetime from 210 to 120 μs (see Table S5 in the ESM) for Yb^{3+} concentrations of 11% and 21%, we obtained k_{Yb_NR} values of 3,760 and 7,190 s^{-1}, respectively (see Table S4 in the ESM). This diminution in lifetime and corresponding increase in k_{Yb_NR} reflects the enhanced energy migration to the UCNPs surface and the increasing number of Yb^{3+} ions at or near the surface, which are prone to quenching by high energy vibrations from surface ligands and solvent molecules [16, 17, 43, 48]. The Yb^{3+}-dependent reduction in Yb^{3+} lifetime goes hand in hand with a reduction in the lifetimes of the green and red Er^{3+} UCL bands from 137 to 85 μs and from 350 to 330 μs, respectively. This is highlighted in Fig. 3 (left panels), summarizing the experimentally determined decay kinetics and the results of our simulation. The lifetimes of the different Er^{3+} bands excited via UC present a combination of the lifetimes of the respective Er^{3+} energy levels obtained by direct Er^{3+} excitation (downshifted (DS) luminescence), and the excited state lifetime of the Yb^{3+} ions feeding these Er^{3+} states via ET, which results in a prolongation of the Er^{3+} lifetimes. As to be expected, the green and red Er^{3+} emission lifetimes obtained upon direct excitation of Er^{3+} are not affected by Yb^{3+} concentration (see Fig. S6 (left panel) in the ESM).

2.1.2 *Er^{3+} concentration series*

The normalized UCL spectra of the Er^{3+} concentration series summarized in Fig. 4(a) show a reduced I_{green} and an enhanced I_{red} with increasing Er^{3+} concentration for P_{unsat} and the opposite behavior for P_{sat}. This observation can explain the different trends of I_{green}/I_{red} reported in literature [32, 33, 36–38]. The I_{green}/I_{red} values presented in Fig. 4(b) seem to be affected by Er^{3+} concentration particularly at P_{unsat}. The broadest P-controlled color tuning range in the spectral region of 546 to 559 nm is observed for UCNPs doped with 14% Yb^{3+} and 1% Er^{3+}. This suggests that a further reduction in Er^{3+} concentration could be advantageous for P-controlled color tuning.

Figure 4(d) highlights a comparison of the measured data and the results of the simulations of $I_{rel,green}(P)$ and $I_{rel,red}(P)$ for the Er^{3+} series. Apparently, an increase in Er^{3+} concentration from 1% to 4% leads to a decrease of $I_{rel,green}(P_{unsat})$ from 54% to 44%, and to an increase of $I_{rel,red}(P_{unsat})$ from 22% to 28%. Simultaneously, $I_{rel,green}(P_{sat})$ increases from 26% to 29% and $I_{rel,red}(P_{sat})$ decreases from 63% to 58%. The P_{cross} values remain unaffected for the chosen Er^{3+} concentrations.

As for the Yb^{3+} series, the $n_{green}(P)$ and $n_{red}(P)$ at low P reveal a biphotonic activation of the green and red Er^{3+} emission bands (see Fig. 4(e)). The onset of saturation of the UC process ($n_{green}(P) = 1.9$) increases from 11 to 20 W·cm^{-2} from 1% to 4% Er^{3+} concentration (see Fig. S7 in the ESM). We attribute the delayed onset of saturation for higher Er^{3+} concentrations to an increasing number of Er^{3+} ions sharing the energy provided by ET from the excited Yb^{3+} ions. The saturation-affected maximum $n_{red}(P)$ of about 2.2 seems to slightly decrease with increasing Er^{3+} concentrations (see Fig. 4(e)). This behavior is ascribed to an enhanced biphotonic activation process of the red emission via the green levels $^2H_{11/2}$ and $^4S_{3/2}$ (k_{NR6}) (see Fig. 1(b)), which are populated via biphotonic processes. This is further supported by the trend of the estimated triphotonic contribution of the population of $^4F_{9/2}$ considering the shape of $n_{red}(P)$, $n_{green}(P)$, and $n_{purple}(P)$ (see Fig. S2 in the ESM).

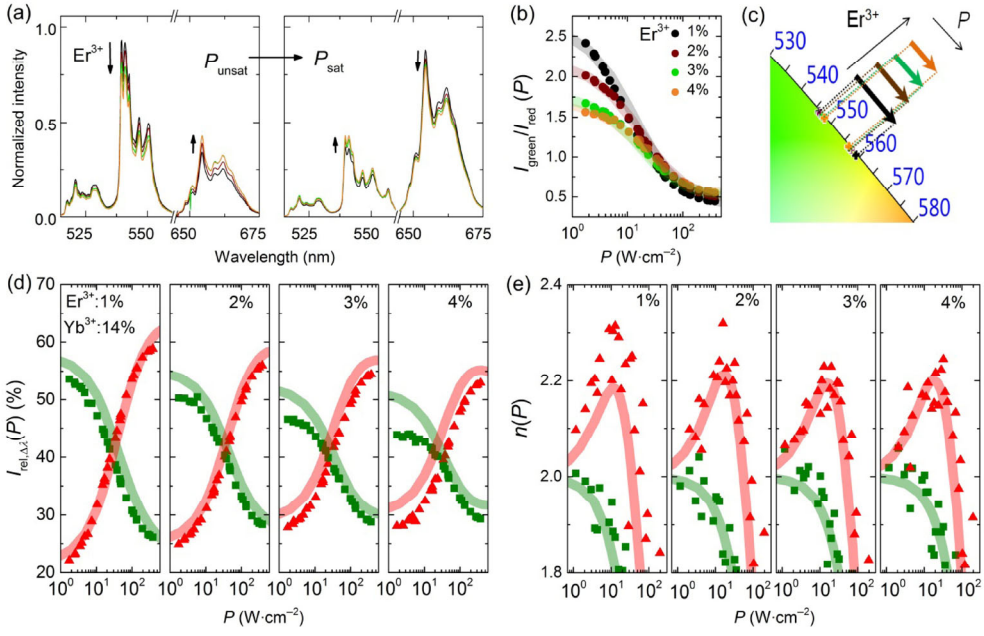

Figure 4 Photoluminescence properties of 33 nm-sized oleate-capped β-$NaYF_4$:Yb^{3+},Er^{3+} UCNPs containing Er^{3+} concentrations between 1% to 4% and a constant Yb^{3+} concentration of 14% dispersed in toluene. (a) UCL spectra shown from 515 to 675 nm for P_{unsat} of 1.8 W·cm^{-2} and P_{sat} of 380 W·cm^{-2}, respectively; all spectra were normalized by division by the total UCL intensity integrated from 370 to 900 nm. (b) *P*-dependent I_{green}/I_{red} values. (c) CIE diagram visualizing the *P*-dependent color tuning range. (d) *P*-dependent relative contribution $I_{rel,\Delta\lambda}(P)$ of the green and red Er^{3+} emission bands to overall UCL. The apparent offset between the measured and simulated $I_{rel,\Delta\lambda}(P)$ values is ascribed to the neglected contribution of the $^4I_{9/2}$ level (810 nm emission band). (e) $n(P)$ values of the green and red Er^{3+} emission. The experimental data are always given as symbols and the results from the simulation of the corresponding parameters or properties with coupled rate equations are provided as lines.

For the simulation of $I_{rel,\Delta\lambda}(P)$ and $n(P)$ of the green and red Er^{3+} emission band and I_{green}/I_{red} of the Er^{3+} concentration series, the following parameters were modified: i) the density of Er^{3+} ions per cm^3, ii) k_{NR} of the $^2F_{5/2}$ level of Yb^{3+} (k_{Yb_NR}), iii) k_{NR} of the $^2H_{11/2}$,$^4S_{3/2}$ level (k_{NR6}), and iv) the depopulation of the red Er^{3+} energy level (see Fig. S4 in the ESM), respectively. Although an increase in Er^{3+} concentration from 1% to 4%, results in a reduction in the average Er^{3+}-Er^{3+} distance from 19.4 to 12.2 Å, the average Er^{3+}-Yb^{3+} distance is barely affected (< 1%, see Appendix C Distances between Yb^{3+} and Er^{3+} ions in the ESM) for the chosen, still relatively low Er^{3+} concentrations. Therefore, ET (Yb^{3+} to Er^{3+}) and BET (Er^{3+} to Yb^{3+}) rate constants are not affected and hence not altered. From the decrease of the 980 nm Yb^{3+} lifetime from 265 to 160 μs (see Fig. 3, right panels), we calculated k_{Yb_NR} values of 2,900 to 5,340 s^{-1} for Er^{3+} concentrations varied from 1% to 4%. Comparing the results obtained for k_{Yb_NR} of the Yb^{3+} series reveals that this value is about twice as sensitive concerning changes of the Er^{3+} concentration. This is attributed to the fact that the energy gap of the 980 nm Er^{3+} level to the next lower lying energy level is about a factor of three smaller than the respective energy gap for the 980 nm Yb^{3+} level. Consequently, the increase in the number of Er^{3+} ions near the UCNPs surface leads to a diminished intensity of particularly the 980 nm Yb^{3+} emission.

The value of k_{NR6} describing the nonradiative depopulation from the green Er^{3+} ($^2H_{11/2}$/$^4S_{3/2}$) to the red Er^{3+} ($^4F_{9/2}$) level increases from 615 to 850 s^{-1} for an increase in Er^{3+} concentration from 1% to 4%. This is also ascribed to faster energy migration to the surface and a higher number of Er^{3+} ions at or close to the particle surface prone to surface quenching. As we kept the rate constant for CR processes constant, this may slightly affect the value of k_{NR6}. These changes in k_{NR6} and k_{Yb_NR} also describe the changes in UCL lifetimes of the green and red Er^{3+} emission rather well, which decrease from 195 to 95 μs and from 350 to 325 μs, respectively, with increasing Er^{3+} concentration (see Fig. 3(b) and Table S5 in the ESM).

The observed decrease of $I_{rel,red}$ at higher *P* with increasing Er^{3+} concentration is ascribed to enhanced Er^{3+}-Er^{3+} interactions. By introducing an additional factor for $k_{ET5\text{-}8}$ depopulating the red Er^{3+} level to the purple level, we used a simplified approach to account for this deactivation process. In order to further optimize the rate analysis, we suggest four possible Er^{3+}-Er^{3+} ET processes, which can play a role involving highly populated excited states depicted in Fig. S4 (k_{UC5a}, k_{UC5b}, k_{UC5c}, k_{UC4}) in the ESM. This includes the resonant $^4I_{11/2}$+$^4F_{9/2}$ → $^4I_{13/2}$+$^2H_{11/2}$ Er^{3+}-Er^{3+} ET process involving the 980 nm-emissive level $^4I_{11/2}$ of Er^{3+}. The rate for this Er^{3+}-Er^{3+} ET, k_{UC5a}, was recently included by the Berry group in their rate equation model [41]. Also, the nonresonant Er^{3+}-Er^{3+} ET k_{UC5b} ($^4I_{13/2}$+$^4F_{9/2}$ → $^4I_{13/2}$+$^2F_{7/2}$) requiring a high population of the $^4I_{13/2}$ energy level due to an energy mismatch of 1,000 cm^{-1} could play a role for the diminution of $I_{rel,red}(P)$ at high *P*. Alternatively, the nonresonant Er^{3+}-Er^{3+} ET rate k_{UC5c} ($^4I_{11/2}$+$^4F_{9/2}$ → $^2H_{11/2}$) with a smaller energy mismatch of about 700 cm^{-1} could be relevant. This rate would compete with the Yb^{3+}-Er^{3+} ET rate $k_{ET5\text{-}8}$ involving the population of $^2H_{9/2}$ via $^4F_{5/2}$ and $^4I_{11/2}$ (see Fig. S4 and Table S2 in the ESM). Another possibility could be a resonant Er^{3+}-Er^{3+} ET ($^4I_{9/2}$+$^4I_{13/2}$ → $^2H_{11/2}$,$^4S_{3/2}$) with a rate constant k_{UC4} feeding the green emission. Such a process was earlier suggested e.g., for purely Er^{3+} systems excited at 1,520 nm employed for solar cell applications as possible population pathway for the green $^2H_{11/2}$,$^4S_{3/2}$ Er^{3+} levels [49, 50]. k_{UC4} was not yet included in the model of the Berry group. In a recent report, we obtained a UC lifetime of 3 ms for the 810 nm $^4I_{9/2}$ of 23 nm-sized $NaYF_4$:Yb^{3+}(20%),Er^{3+}(2%) UCNPs in D_2O indicating a high population of this level. It is noteworthy that the prolongation of this UC lifetime by Yb^{3+} feeding can be excluded, as the lifetime of the 980 nm emission of Yb^{3+} was determined to be only 42 μs in this report. Possibly, the UC lifetime of the Er^{3+} 810 nm energy level was prolonged by feeding from the Er^{3+} 1,520 nm energy level. Also, the *P*-dependent decrease of the relative intensity contribution of the 810 nm emission band (see Fig. S3 in the ESM) points towards k_{UC4} being a promising candidate for further optimizing the rate equation analysis. Additionally, our results suggest that the CR processes proposed by Vetrone et al. ($^4F_{7/2}$ + $^4I_{11/2}$ → $^4F_{9/2}$ + $^4F_{9/2}$) [51] and Gao et al. ($^4I_{13/2}$ + $^2H_{11/2}$,$^4S_{3/2}$ → $^4I_{11/2}$ + $^4F_{9/2}$) [52] are less likely to apply for our UCNPs systems, as both should lead to an increase of the red emission at high *P* for

increasing Er^{3+} concentrations. A deeper understanding of these activation and deactivation processes of the red Er^{3+} emission band could be achieved by the challenging simultaneous excitation at 980 and 1,550 nm over a broad P range. Recently, Zhang et al. reported on the unexpected stimulated emission depletion (STED) process in Yb^{3+}, Tm^{3+} based UCNPs for simultaneous excitation at 980 and 1,550 nm [53].

2.2 Upconversion quantum yield ($\Phi_{UC}(P)$) and particle brightness ($B_{UC}(P)$)

To assess the UC performance of our UCNPs, we obtained the P-dependent Φ_{UC} for the Yb^{3+} and Er^{3+} concentration series over a P-range of more than two orders of magnitude. This also includes the maximum values of Φ_{UC} ($\Phi_{UC,max}$), see Figs. 5(a) and 5(b) where $n_{green}(P)$ reaches 1. The differences in Φ_{UC} are most pronounced for low P and decrease with increasing P exceeding 10 W·cm^{-2}, due to at least partial compensation of nonradiative processes by high P. For all samples, $\Phi_{UC,max}$ was reached at about P of 380 W·cm^{-2}. The highest $\Phi_{UC,max}$ with values of about 2.5% were obtained for the β-$NaYF_4$: 14% Yb^{3+}, 1% Er^{3+} nanoparticles (see Table 1). To highlight differences in performance of the studied UCNPs all $\Phi_{UC}(P)$ values were normalized to this $\Phi_{UC}(P)$ (see Fig. 5(b)). The smallest $\Phi_{UC}(P)$ values gave β-$NaYF_4$: 21% Yb^{3+}, 3% Er^{3+} UCNPs and β-$NaYF_4$: 14% Yb^{3+}, 4% Er^{3+} UCNPs with 53% and 40% at low P (see Fig. 5(c)).

For UCNPs, the size of the eventually detected upconversion signal is determined by particle brightness ($B_{UC}(P)$), i.e., by the product of the $\Phi_{UC}(P)$ and the absorption cross section of the UCNPs at the used excitation wavelength. The considerably smaller absorption coefficient of the less abundant Er^{3+} ions at 976 nm is neglected for this calculation. Assuming a volume of the unit cell of β-$NaYF_4$ of about 0.109 nm^3 with 1.5 Y^{3+} ions per unit cell yields about 28,700 (11% Yb^{3+}) up to 55,500 (21% Yb^{3+}) absorbing Yb^{3+} ions per particle. With an absorption cross section of 1.2×10^{-20} cm^2 per Yb^{3+} ion at 974 nm, as determined for Al_2O_3 waveguides [54], this gives maximum B_{UC} values between 0.8×10^{-17} and 1.2×10^{-17} cm^2 for P_{sat} = 380 W·cm^{-2} (see Table 1). The corresponding B_{UC} values for P_{unsat} = 1.8 W·cm^{-2} are about a factor of 100 smaller. Normalization of the B_{UC} values of the Yb^{3+} and Er^{3+} series to the highest B_{UC} values obtained for P_{unsat} of 1.8 W·cm^{-2} and P_{sat} of 380 W·cm^{-2} gives the relative B_{UC} values, shown in Figs. 5(d) and 5(e). This also addresses the influence of P on B_{UC}. As shown in Fig. 5(d), the maximum B_{UC} of our particle series was found for UCNPs doped with 14% Yb^{3+} and 3% Er^{3+} for P_{unsat}. In contrast, for P_{sat}, the B_{UC} values of the UCNPs steadily increase with increasing Yb^{3+} concentration. The trend observed for P_{sat} underlines the dominant influence of the UCNPs absorption cross section, which is determined by the number of Yb^{3+} ions per particle. This parameter can compensate for lower Φ_{UC}, as revealed by the maximum B_{UC} value obtained for the least emissive (lowest Φ_{UC}) UCNPs doped with 21% Yb^{3+} and 3% Er^{3+}. Even higher B_{UC} values are to be expected for higher Yb^{3+} concentrations, with the optimum Yb^{3+} concentration depending on UCNPs size and particle architecture covering the parameters core vs. core-shell structures, shell thickness and tightness as well as the spatial arrangement of the different lanthanide dopant ions [12, 39, 42, 43]. For our Yb^{3+},Er^{3+}-co-doped UCNPs, an enhanced Yb^{3+} concentration favors, however, also automatically a higher contribution of the red Er^{3+} emission to overall UCL, as previously detailed. This can be counterproductive for certain applications, where a different emission

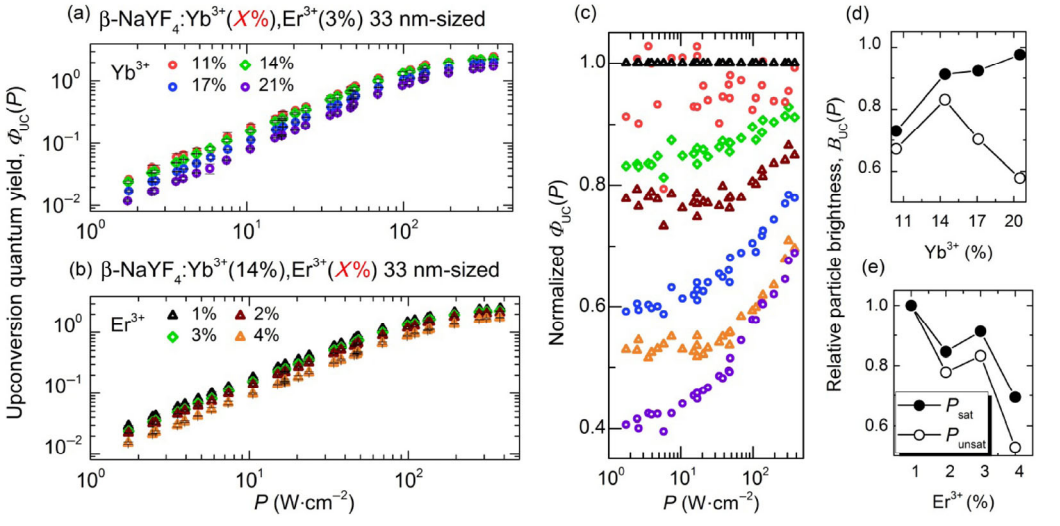

Figure 5 P-dependent $\Phi_{UC}(P)$ for (a) the Yb^{3+} and (b) the Er^{3+} series of 33 nm-sized oleate-capped β-$NaYF_4$:Yb^{3+},Er^{3+} UCNPs dispersed in toluene. (c) $\Phi_{UC}(P)$ curves normalized to the $\Phi_{UC}(P)$ of optimum emissive β-$NaYF_4$: 14% Yb^{3+},1% Er^{3+} UCNPs, and relative B_{UC} values for (d) the Yb^{3+} and (e) the Er^{3+} series of these UCNPs, normalized to the highest B_{UC} values obtained for P_{sat} (full symbols) and P_{unsat} (open symbols), respectively.

Table 1 Φ_{UC} of the Yb^{3+} and Er^{3+} concentration series of 33 nm-sized oleate-capped $NaYF_4$:Yb^{3+},Er^{3+} UCNPs dispersed in toluene obtained at P of 20 and 380 W·cm^{-2} and $B_{UC,max}$ for P of 380 W·cm^{-2} for an excitation wavelength of 976.4 nm. Φ_{UC} of the green and red emission that account for at least 80% of the UCL compared to overall UCL from 370–900 nm

β-$NaYF_4$:Yb^{3+},Er^{3+}(%), (%)	Φ_{UC}@20 W·cm^{-2} (%)	$\Phi_{UC,max}$@380 W·cm^{-2} (%)	$B_{UC,max}$@380 W·cm^{-2} (cm^2)
11, 3	0.34	2.50	0.86×10^{-17}
14, 3	0.30	2.30	1.08×10^{-17}
17, 3	0.22	1.96	1.09×10^{-17}
21, 3	0.16	1.73	1.15×10^{-17}
14, 1	0.35	2.52	1.18×10^{-17}
14, 2	0.27	2.13	1.08×10^{-17}
14, 4	0.18	1.75	0.82×10^{-17}

color, a higher contribution of other emission bands, and/or more extensive color tuning are required. Recently, other research groups reported the advantages of very highly doped systems as tools for microscopic studies using P values in the range of > 10^6 W·cm^{-2} [55]. Shen et al. [35] showed that for 9 nm-sized α-$NaYF_4$:Yb^{3+}, Er^{3+}(2%) UCNPs with an 5 nm thick inactive CaF_2 shell, an Yb^{3+} concentration as high as 98% is optimum for maximum B_{UC} for a P of 30 W·cm^{-2} and Gargas et al. [56] showed that sub 10 nm-sized $NaYF_4$ UCNPs doped with 20% Yb^{3+} and 20% Er^{3+} reveal a superior performance for $P > 3 \times 10^5$ W·cm^{-2}, compared to UCNPs with dopant concentrations of 20% Yb^{3+} and only 2% Er^{3+}. For applications, requiring low P in the range of 1 W·cm^{-2}, conventionally doped UCNPs with less Yb^{3+} and Er^{3+} concentration of about 20% and 2%, respectively, still perform much better than the highly doped UCNPs systems.

3 Conclusions and outlook

In summary, we quantified the influence of the Yb^{3+} and Er^{3+} concentration on the relative spectral distribution and emission color, quantum yield (Φ_{UC}), and luminescence decay kinetics of the upconversion luminescence (UCL) and the signal determining particle brightness (B_{UC}) of a set of 33 nm-sized, uniformly doped, oleate-capped core-only β-$NaYF_4$:Yb^{3+}, Er^{3+} dispersed in toluene for Yb^{3+} and Er^{3+} concentrations varied between 11%–21% and 1%–4%, respectively. These parameters were assessed over a broad range of excitation power densities (P), covering more than two orders of magnitude. To support mechanistic conclusions, the UCL properties were simulated with a nine-level Er^{3+} rate equation model [14, 41] using modified rate constants. The combination of such a large set of parameters as the excitation power density-dependent emission intensities of the different Er^{3+} bands, Yb^{3+} and Er^{3+} lifetimes, and Yb^{3+} and Er^{3+} dopant concentrations for the fitting of experimentally determined data has not been done previously for optimizing rate equation constants.

The influence of the Yb^{3+} concentration on the relative spectral distribution of UCL originates primarily from changes of the energy transfer (ET) and back-energy transfer (BET) rates. The enhancement of the red emission intensity observed at high P was attributed to an enhancement of the triphotonic activation of the $^4F_{9/2}$ energy level by the $^4G_{11/2} \rightarrow {}^4F_{9/2}$ BET process. The amplification of the triphotonic activation of the red Er^{3+} emission was quantified with the aid of the P-dependent slope factors $n(P)$'s of the different emission bands. Investigating the influence of the Er^{3+} concentration for the Er^{3+} series revealed an increase of the biphotonic activation of the red emissive Er^{3+} level caused by an enhanced nonradiative relaxation rate from the green energy level (k_{NR6}). The diminished intensity of the red emission at high P can be accounted for by implementing an Er^{3+}-Er^{3+} ET rate in the rate equation model used. With the theoretical analysis of the experimentally derived UCL characteristics we could quantify changes in effective ET processes due to a reduction in the distances of the interacting optically active lanthanide ions.

Overall, our results present an important step for the design of UCNPs with high color purity of their emission as well as for the rational tuning of the relative spectral distribution of UCL and signal size. Especially important with respect to the screening approaches for the rational design of UCNPs developed e.g., by Chan et al. [7], our studies underline the strong P-dependence of the color output and color tuning range for different concentrations of the optically active lanthanide dopant ions. Additionally, we demonstrated that the P value where $I_{rel,green}(P)$ and $I_{rel,red}(P)$ cross (P_{cross}), suggested as simply accessible performance parameter for UCNPs [42], can be exploited as a screening parameter for UCL efficiency only for materials with comparable Yb^{3+} and Er^{3+} dopant concentrations. Our results underline that there is still place for optimization of the dopant ion concentrations regarding the size of Φ_{UC}; in this respect, in the future we will study smaller Er^{3+} dopant concentrations and higher Yb^{3+} concentrations in core-only and core-shell nanostructures with inactive and active shells.

In general, a compromise needs to be found for the concentration of the sensitizer Yb^{3+}, that boost the absorption of the excitation light and thus B_{UC}, and the need, to simultaneously minimizing energy dissipation to the particle surface, where surface quenching can occur without a passivation shell. The Er^{3+} concentration must be optimized to minimize unfavorable cross relaxation (CR) processes. As to be expected from our results, higher Yb^{3+} and lower Er^{3+} concentration will boost UCNPs brightness at low P, whereas for high P applications, highly doped UCNPs seem to be advantageous.

4 Material and methods

4.1 UCNPs

Uniformly 33.5 ± 0.5 nm-sized oleate-capped β-$NaYF_4$:Yb^{3+},Er^{3+} UCNPs were prepared via a previously described synthesis method from Ylihärsilä [57] with small modifications. All samples were characterized regarding size and size distribution, crystal phase, and dopant ion concentration using transmission electron microscopy (TEM), X-ray diffraction (XRD), inductively coupled optical emission spectroscopy (ICP-OES). The absorbance spectra, recorded on a calibrated Cary 5000 spectrometer, show absence of scattering at the excitation wavelength (see Appendix A, Fig. S1 and Table S1 in the ESM).

4.2 Time-resolved luminescence measurements

Luminescence UC lifetime measurements of the in toluene dispersed UCNPs samples were carried out with a commercial Edinburgh Instruments spectrofluorometer FSP-920 equipped with an electrically pulsed 1 W 978 nm laser diode with a 950 μs long square pulse. The pulse energy of the 978 nm laser pulses was about 1 mJ·cm^{-2}. In addition, a pulsed xenon lamp (pulse width of about 1 μs) was used for time-resolved measurements of the DS emission of Yb^{3+} and Er^{3+}. The signal was detected with a red extended PMT (R2658P) and a NIR PMT (R5509P) from Hamamatsu. We determined UCL decays of the 410, 540, and 655 nm Er^{3+} emission bands and the DSL decay of Er^{3+} 410, 540, 655, and 1,520 nm emission bands as well the DSL decay of the 980 nm Yb^{3+} emission (see Fig. S6 and Table S5 in the ESM).

4.3 Absolute measurement of Φ_{UC} and UCL

P-dependent Φ_{UC} values of the UCNPs dispersed in toluene were obtained absolutely with a custom-designed integrating sphere setup previously reported [17], using a high stability 8 W 976 nm laser diode as excitation light source. The measurements were performed with a well-characterized a top hat (TH) beam profile with a spot diameter of 1.4 mm, previously reported [17]. The intensity averaged wavelength of the laser diode was adjusted to 976.4 nm, which is resonant to the Yb^{3+} absorption peak. P was controlled with two filter wheels equipped with reflective neutral density filters and thereby varied over 2–3 orders of magnitude. P was directly measured with the calibrated integrating sphere setup for every single Φ_{UC} value using a solvent filled cuvette. The calibration of the wavelength scale and the range of linearity of the setup were performed following previously described procedures [58–61]. All UCL spectra were multiplied with λ/hc_0 to obtain spectral photon fluxes (s^{-1}·m^{-3}) [62], thus also the $I_{rel,\Delta\lambda}(P)$ and I_{green}/I_{red} were calculated with this unit. For the calculation of Φ_{UC} all UC photons in the wavelength region from 370–900 nm were considered and divided by the number of absorbed photons. The UCNPs dispersions were filled in 4 mm × 10 mm (width × length) quartz cuvettes from Hellma to circumvent reabsorption and indirect excitation in the integrating sphere by

photons diffusively reflected from the sphere walls. For the absorbance measurements an optical path length of 4 mm was used and for the Φ_{UC} an optical path length of 10 mm (in excitation). As blank sample we used a cuvette filled only with the solvent. The measurement time was set to 30 s to reduce heating effects and all measurements were repeated at least four times. To guarantee accurate Φ_{UC} measurements, the absorbances of all UCNPs samples at the excitation wavelength of 980 nm (except for one sample) were chosen to be large enough to compensate for uncertainties introduced in the measurement of the number of absorbed photons at the excitation wavelength by small fluctuations of the laser diode (see Fig. S1 in the ESM). The stability of the laser diode was 0.1%. We did not correct the Φ_{UC} values for contributions from the Yb^{3+} emission that was very weak for the samples studied.

4.4 Integration intervals for emission bands

We chose the following integration intervals for the determination of the relative spectral UC intensity, which are required for the calculation of $I_{rel,\Delta\lambda}(P)$, $I_{green}/I_{red}(P)$ and $n(P)$ (see Eq. (1)).

Table 2 Integration intervals for discussed electronic transitions

$\Delta\lambda$	Electronic transition	Integration interval (nm)
Purple	$^2H_{9/2} \rightarrow {}^4I_{15/2}$	394–430
Green	$^2H_{11/2}$, $^4S_{3/2} \rightarrow {}^4I_{15/2}$	510–570
Red	$^4F_{9/2} \rightarrow {}^4I_{15/2}$	630–685
NIR (810 nm)	$^4I_{9/2} \rightarrow {}^4I_{15/2}$	783–833
Overall UCL intensity		370–900

4.5 Calculation of slope factors $n(P)$

The P-dependent slope factors ($n(P)$) were calculated with the neigbouring experimentally determined intensity data points $I(P_i)$ and $I(P_j)$ with Eq. (1)

$$n(P) = \frac{\ln\left(I(P_j)\right) - \ln\left(I(P_i)\right)}{\ln(P_j) - \ln(P_i)} \quad (1)$$

4.6 CIE color coordinates

CIE graphs in the CIE2015 10° x,y color space were created with the ColorCalculator 7.19 tool from OSRAM Sylvania Inc. (https://www.osram.us/cb/tools-and-resources/applications/led-colorcalculator/index.jsp)

Acknowledgements

Synthesis of the UCNPs by Emilia Palo and performance of the ICP-OES measurements by MSc. Melissa Monks is gratefully acknowledged. URG acknowledges financial support by research grants RE 1203/18-1 (German research council; DFG), RE 1203/20-1 (project NANOHYPE; DFG and M-Eranet) and TS from Tekes, the Finnish Funding Agency for Innovation.

Electronic Supplementary Material: Supplementary material (characterization of UCNPs with TEM, XRD, and absorption spectroscopy, time resolved data, calculation of the triphotonic population contribution of the red emission band, description of fitting procedure, results of rate equation analysis) is available in the online version of this article at https://doi.org/10.1007/s12274-019-2450-4.

References

[1] Mader, H. S.; Kele, P.; Saleh, S. M.; Wolfbeis, O. S. Upconverting luminescent nanoparticles for use in bioconjugation and bioimaging. *Curr. Opin. Chem. Biol.* **2010**, *14*, 582–596.

[2] Goldschmidt, J. C.; Fischer, S. Upconversion for photovoltaics - a review of materials, devices and concepts for performance enhancement. *Adv. Opt. Mater.* **2015**, *3*, 510–535.

[3] Chen, G. Y.; Ågren, H.; Ohulchanskyy, T. Y.; Prasad, P. N. Light upconverting core-shell nanostructures: Nanophotonic control for emerging applications. *Chem. Soc. Rev.* **2015**, *44*, 1680–1713.

[4] Resch-Genger, U.; Gorris, H. H. Perspectives and challenges of photon-upconversion nanoparticles - Part I: Routes to brighter particles and quantitative spectroscopic studies. *Anal. Bioanal. Chem.* **2017**, *409*, 5855–5874.

[5] Jaque, D.; Vetrone, F. Luminescence nanothermometry. *Nanoscale* **2012**, *4*, 4301–4326.

[6] Zhou, B.; Shi, B. Y.; Jin, D. Y.; Liu, X. G. Controlling upconversion nanocrystals for emerging applications. *Nat. Nanotechnol.* **2015**, *10*, 924–936.

[7] Chan, E. M. Combinatorial approaches for developing upconverting nanomaterials: High-throughput screening, modeling, and applications. *Chem. Soc. Rev.* **2015**, *44*, 1653–1679.

[8] Haase, M.; Schafer, H. Upconverting nanoparticles. *Angew. Chem., Int. Ed.* **2011**, *50*, 5808–5829.

[9] Liu, G. K. Advances in the theoretical understanding of photon upconversion in rare-earth activated nanophosphors. *Chem. Soc. Rev.* **2015**, *44*, 1635–1652.

[10] Han, S. Y.; Deng, R. R.; Xie, X. J.; Liu, X. G. Enhancing luminescence in lanthanide-doped upconversion nanoparticles. *Angew. Chem., Int. Ed.* **2014**, *53*, 11702–11715.

[11] Wang, X. D.; Valiev, R. R.; Ohulchanskyy, T. Y.; Ågren, H.; Yang, C. H.; Chen, G. Y. Dye-sensitized lanthanide-doped upconversion nanoparticles. *Chem. Soc. Rev.* **2017**, *46*, 4150–4167.

[12] Pilch, A.; Würth, C.; Kaiser, M.; Wawrzyńczyk, D.; Kurnatowska, M.; Arabasz, S.; Prorok, K.; Samoć, M.; Strek, W.; Resch-Genger, U. et al. Shaping luminescent properties of Yb^{3+} and Ho^{3+} co-doped upconverting core–shell β-$NaYF_4$ nanoparticles by dopant distribution and spacing. *Small* **2017**, *13*, 1701635.

[13] Renero-Lecuna, C.; Martín-Rodríguez, R.; Valiente, R.; González, J.; Rodríguez, F.; Krämer, K. W.; Güdel, H. U. Origin of the high upconversion green luminescence efficiency in β-$NaYF_4$:2%Er^{3+},20%Yb^{3+}. *Chem. Mater.* **2011**, *23*, 3442–3448.

[14] Anderson, R. B.; Smith, S. J.; May, P. S.; Berry, M. T. Revisiting the NIR-to-visible upconversion mechanism in β-$NaYF_4$:Yb^{3+},Er^{3+}. *J. Phys. Chem. Lett.* **2014**, *5*, 36–42.

[15] Berry, M. T.; May, P. S. Disputed mechanism for NIR-to-red upconversion luminescence in $NaYF_4$:Yb^{3+},Er^{3+}. *J. Phys. Chem. A* **2015**, *119*, 9805–9811.

[16] Würth, C.; Kaiser, M.; Wilhelm, S.; Grauel, B.; Hirsch, T.; Resch-Genger, U. Excitation power dependent population pathways and absolute quantum yields of upconversion nanoparticles in different solvents. *Nanoscale* **2017**, *9*, 4283–4294.

[17] Kaiser, M.; Würth, C.; Kraft, M.; Hyppänen, I.; Soukka, T.; Resch-Genger, U. Power-dependent upconversion quantum yield of $NaYF_4$:Yb^{3+},Er^{3+} nano- and micrometer-sized particles-measurements and simulations. *Nanoscale* **2017**, *9*, 10051–10058.

[18] Wang, F.; Liu, X. G. Upconversion multicolor fine-tuning: Visible to near-infrared emission from lanthanide-doped $NaYF_4$ nanoparticles. *J. Am. Chem. Soc.* **2008**, *130*, 5642–5643.

[19] Wang, J.; Deng, R. R.; MacDonald, M. A.; Chen, B. L.; Yuan, J. K.; Wang, F.; Chi, D. Z.; Andy Hor, T. S.; Zhang, P.; Liu, G. K. et al. Enhancing multiphoton upconversion through energy clustering at sublattice level. *Nat. Mater.* **2014**, *13*, 157–162.

[20] Gao, D. L.; Zhang, X. Y.; Chong, B.; Xiao, G. Q.; Tian, D. P. Simultaneous spectra and dynamics processes tuning of a single upconversion microtube through Yb^{3+} doping concentration and excitation power. *Phys. Chem. Chem. Phys.* **2017**, *19*, 4288–4296.

[21] Zhou, J.; Liu, Q.; Feng, W.; Sun, Y.; Li, F. Y. Upconversion luminescent materials: Advances and applications. *Chem. Rev.* **2015**, *115*, 395–1465.

[22] Xue, X. J.; Uechi, S.; Tiwari, R. N.; Duan, Z. C.; Liao, M. S.; Yoshimura, M.; Suzuki, T.; Ohishi, Y. Size-dependent upconversion luminescence and quenching mechanism of $LiYF_4$: Er^{3+}/Yb^{3+} nanocrystals with oleate ligand adsorbed. *Opt. Mater. Express* **2013**, *3*, 989–999.

[23] Xu, C. T.; Zhan, Q. Q.; Liu, H. C.; Somesfalean, G.; Qian, J.; He, S. L.; Andersson-Engels, S. Upconverting nanoparticles for pre-clinical diffuse optical imaging, microscopy and sensing: Current trends and future challenges. *Laser Photonics Rev.* **2013**, *7*, 663–697.

[24] Wei, W.; Zhang, Y.; Chen, R.; Goggi, J.; Ren, N.; Huang, L.; Bhakoo, K. K.; Sun, H. D.; Tan, T. T. Y. Cross relaxation induced pure red upconversion

in activator- and sensitizer-rich lanthanide nanoparticles. *Chem. Mater.* **2014**, *26*, 5183–5186.

[25] Wang, Y.; Liu, K.; Liu, X. M.; Dohnalová, K.; Gregorkiewicz, T.; Kong, X. G.; Aalders, M. C. G.; Buma, W. J.; Zhang, H. Critical shell thickness of core/shell upconversion luminescence nanoplatform for FRET application. *J. Phys. Chem. Lett.* **2011**, *2*, 2083–2088.

[26] Wang, F.; Liu, X. G. Recent advances in the chemistry of lanthanide-doped upconversion nanocrystals. *Chem. Soc. Rev.* **2009**, *38*, 976–989.

[27] Wang, F.; Han, Y.; Lim, C. S.; Lu, Y. H.; Wang, J.; Xu, J.; Chen, H. Y.; Zhang, C.; Hong, M. H.; Liu, X. G. Simultaneous phase and size control of upconversion nanocrystals through lanthanide doping. *Nature* **2010**, *463*, 1061–1065.

[28] Vetrone, F.; Naccache, R.; Mahalingam, V.; Morgan, C. G.; Capobianco, J. A. The active-core/active-shell approach: A strategy to enhance the upconversion luminescence in lanthanide-doped nanoparticles. *Adv. Funct. Mater.* **2009**, *19*, 2924–2929.

[29] Bogdan, N.; Vetrone, F.; Ozin, G. A.; Capobianco, J. A. Synthesis of ligand-free colloidally stable water dispersible brightly luminescent lanthanide-doped upconverting nanoparticles. *Nano Lett.* **2011**, *11*, 835–840.

[30] Arppe, R.; Hyppänen, I.; Perälä, N.; Peltomaa, R.; Kaiser, M.; Würth, C.; Christ, S.; Resch-Genger, U.; Schaferling, M.; Soukka, T. Quenching of the upconversion luminescence of $NaYF_4$:Yb^{3+},Er^{3+} and $NaYF_4$:Yb^{3+},Tm^{3+} nanophosphors by water: The role of the sensitizer Yb^{3+} in non-radiative relaxation. *Nanoscale* **2015**, *7*, 11746–11757.

[31] Liu, L.; Jiang, H. L.; Chen, Y. J.; Zhang, X. L.; Zhang, Z. G.; Wang, Y. X. Power dependence of upconversion luminescence of Er^{3+} doped Yttria nanocrystals and their bulk counterpart. *J. Lumin.* **2013**, *143*, 423–431.

[32] Mai, H. X.; Zhang, Y. W.; Sun, L. D.; Yan, C. H. Size- and phase-controlled synthesis of monodisperse $NaYF_4$:Yb,Er nanocrystals from a unique delayed nucleation pathway monitored with upconversion spectroscopy. *J. Phys. Chem. C* **2007**, *111*, 13730–13739.

[33] Xu, D. K.; Liu, C. F.; Yan, J. W.; Yang, S. H.; Zhang, Y. L. Understanding energy transfer mechanisms for tunable emission of Yb^{3+}-Er^{3+} codoped GdF_3 nanoparticles: Concentration-dependent luminescence by near-infrared and violet excitation. *J. Phys. Chem. C* **2015**, *119*, 6852–6860.

[34] Liao, J. S.; Nie, L. L.; Liu, S. H.; Liu, B.; Wen, H. R. Yb^{3+} concentration dependence of upconversion luminescence in $Y_2Sn_2O_7$:Yb^{3+}/Er^{3+} nanophosphors. *J. Mater. Sci.* **2014**, *49*, 6081–6086.

[35] Shen, B.; Cheng, S. M.; Gu, Y. Y.; Ni, D. R.; Gao, Y. L.; Su, Q. Q.; Feng, W.; Li, F. Y. Revisiting the optimized doping ratio in core/shell nanostructured upconversion particles. *Nanoscale* **2017**, *9*, 1964–1971.

[36] Zhao, J. W.; Sun, Y. J.; Kong, X. G.; Tian, L. J.; Wang, Y.; Tu, L. P.; Zhao, J. L.; Zhang, H. Controlled synthesis, formation mechanism, and great enhancement of red upconversion luminescence of $NaYF_4$:Yb^{3+},Er^{3+} nanocrystals/submicroplates at low doping level. *J. Phys. Chem. B* **2008**, *112*, 15666–15672.

[37] Zhu, H. Y.; Lin, M.; Jin, G. R.; Lu, T. J.; Xu, F. A modified energy transfer model for determination of upconversion emission of β-$NaYF_4$:Yb,Er: Role of self-quenching effect. *J. Lumin.* **2017**, *185*, 292–297.

[38] Li, D. G.; Qin, W. P.; Zhao, D.; Aidilibike, T.; Chen, H.; Liu, S. H.; Zhang, P.; Wang, L. L. Tunable green to red upconversion fluorescence of water-soluble hexagonal-phase core-shell CaF_2@$NaYF_4$ nanocrystals. *Opt. Mater. Express* **2016**, *6*, 270–278.

[39] Kraft, M.; Würth, C.; Muhr, V.; Hirsch, T.; Resch-Genger, U. Particle-size-dependent upconversion luminescence of $NaYF_4$: Yb, Er nanoparticles in organic solvents and water at different excitation power densities. *Nano Res.* **2018**, *11*, 6360–6374.

[40] Fischer, S.; Bronstein, N. D.; Swabeck, J. K.; Chan, E. M.; Alivisatos, A. P. Precise tuning of surface quenching for luminescence enhancement in core–shell lanthanide-doped nanocrystals. *Nano Lett.* **2016**, *16*, 7241–7247.

[41] Hossan, M. Y.; Hor, A.; Luu, Q.; Smith, S. J.; May, P. S.; Berry, M. T. Explaining the nanoscale effect in the upconversion dynamics of β-$NaYF_4$:Yb^{3+}, Er^{3+} core and core-shell nanocrystals. *J. Phys. Chem. C* **2017**, *121*, 16592–16606.

[42] Homann, C.; Krukewitt, L.; Frenzel, F.; Grauel, B.; Würth, C.; Resch-Genger, U.; Haase, M. $NaYF_4$:Yb,Er/$NaYF_4$ core/shell nanocrystals with high upconversion luminescence quantum yield. *Angew. Chem., Int. Ed.* **2018**, *57*, 8765–8769.

[43] Würth, C.; Fischer, S.; Grauel, B.; Alivisatos, A. P.; Resch-Genger, U. Quantum yields, surface quenching, and passivation efficiency for ultrasmall core/shell upconverting nanoparticles. *J. Am. Chem. Soc.* **2018**, *140*, 4922–4928.

[44] Zhao, J. B.; Lu, Z. D.; Yin, Y. D.; McRae, C.; Piper, J. A.; Dawes, J. M.; Jin, D. Y.; Goldys, E. M. Upconversion luminescence with tunable lifetime in $NaYF_4$:Yb,Er nanocrystals: Role of nanocrystal size. *Nanoscale* **2013**, *5*, 944–952.

[45] Wilhelm, S.; Kaiser, M.; Würth, C.; Heiland, J.; Carrillo-Carrion, C.; Muhr, V.; Wolfbeis, O. S.; Parak, W. J.; Resch-Genger, U.; Hirsch, T. Water dispersible upconverting nanoparticles: Effects of surface modification on their luminescence and colloidal stability. *Nanoscale* **2015**, *7*, 1403–1410.

[46] Hudry, D.; Busko, D.; Popescu, R.; Gerthsen, D.; Abeykoon, A. M. M.; Kübel, C.; Bergfeldt, T.; Richards, B. S. Direct evidence of significant cation intermixing in upconverting core@shell nanocrystals: Toward a new crystallochemical model. *Chem. Mater.* **2017**, *29*, 9238–9246.

[47] Dühnen, S.; Haase, M. Study on the intermixing of core and shell in $NaEuF_4$/$NaGdF_4$ core/shell nanocrystals. *Chem. Mater.* **2015**, *27*, 8375–8386.

[48] Zuo, J.; Sun, D. P.; Tu, L. P.; Wu, Y. N.; Cao, Y. H.; Xue, B.; Zhang, Y. L.; Chang, Y. L.; Liu, X. M.; Kong, X. G. et al. Precisely tailoring upconversion dynamics via energy migration in core–shell nanostructures. *Angew. Chem., Int. Ed.* **2018**, *57*, 3054–3058.

[49] Shalav, A.; Richards, B. S.; Trupke, T.; Krämer, K. W.; Güdel, H. U. Application of $NaYF_4$:Er^{3+} up-converting phosphors for enhanced near-infrared silicon solar cell response. *Appl. Phys. Lett.* **2004**, *86*, 013505.

[50] Ivaturi, A.; MacDougall, S. K. W.; Martín-Rodríguez, R.; Quintanilla, M.; Marques-Hueso, J.; Krämer, K. W.; Meijerink, A.; Richards, B. S. Optimizing infrared to near infrared upconversion quantum yield of β-$NaYF_4$:Er^{3+} in fluoropolymer matrix for photovoltaic devices. *J. Appl. Phys.* **2013**, *114*, 013505.

[51] Vetrone, F.; Boyer, J. C.; Capobianco, J. A.; Speghini, A.; Bettinelli, M. Effect of Yb^{3+} codoping on the upconversion emission in nanocrystalline Y_2O_3:Er^{3+}. *J. Phys. Chem. B* **2003**, *107*, 1107–1112.

[52] Gao, D. L.; Zhang, X. Y.; Zheng, H. R.; Gao, W.; He, E. J. Yb^{3+}/Er^{3+} codoped β-$NaYF_4$ microrods: Synthesis and tuning of multicolor upconversion. *J. Alloys Compd.* **2013**, *554*, 395–399.

[53] Zhang, H. X.; Jia, T. Q.; Chen, L.; Zhang, Y. C.; Zhang, S. A.; Feng, D. H.; Sun, Z. R.; Qiu, J. R. Depleted upconversion luminescence in $NaYF_4$:Yb^{3+},Tm^{3+} nanoparticles via simultaneous two-wavelength excitation. *Phys. Chem. Chem. Phys.* **2017**, *19*, 17756–17764.

[54] Strohhöfer, C.; Polman, A. Absorption and emission spectroscopy in Er^{3+}–Yb^{3+} doped aluminum oxide waveguides. *Opt. Mater.* **2003**, *21*, 705–712.

[55] Wen, S. H.; Zhou, J. J.; Zheng, K. Z.; Bednarkiewicz, A.; Liu, X. G.; Jin, D. Y. Advances in highly doped upconversion nanoparticles. *Nat. Commun.* **2018**, *9*, 2415.

[56] Gargas, D. J.; Chan, E. M.; Ostrowski, A. D.; Aloni, S.; Altoe, M. V. P.; Barnard, E. S.; Sanii, B.; Urban, J. J.; Milliron, D. J.; Cohen, B. E. et al. Engineering bright sub-10-nm upconverting nanocrystals for single-molecule imaging. *Nat. Nanotechnol.* **2014**, *9*, 300–305.

[57] Ylihärsilä, M.; Harju, E.; Arppe, R.; Hattara, L.; Hölsä, J.; Saviranta, P.; Soukka, T.; Waris, M. Genotyping of clinically relevant human adenoviruses by array-in-well hybridization assay. *Clin. Microbiol. Infect.* **2013**, *19*, 551–557.

[58] Würth, C.; Grabolle, M.; Pauli, J.; Spieles, M.; Resch-Genger, U. Comparison of methods and achievable uncertainties for the relative and absolute measurement of photoluminescence quantum yields. *Anal. Chem.* **2011**, *83*, 3431–3439.

[59] Würth, C.; Pauli, J.; Lochmann, C.; Spieles, M.; Resch-Genger, U. Integrating sphere setup for the traceable measurement of absolute photoluminescence quantum yields in the near infrared. *Anal. Chem*, **2012**, *84*, 1345–1352.

[60] Hatami, S.; Würth, C.; Kaiser, M.; Leubner, S.; Gabriel, S.; Bahrig, L.; Lesnyak, V.; Pauli, J.; Gaponik, N.; Eychmüller, A. et al. Absolute photoluminescence quantum yields of IR26 and IR-emissive $Cd_{1-x}Hg_xTe$ and PbS quantum dots - method- and material-inherent challenges. *Nanoscale* **2015**, *7*, 133–143.

[61] Resch-Genger, U.; Bremser, W.; Pfeifer, D.; Spieles, M.; Hoffmann, A.; DeRose, P. C.; Zwinkels, J. C.; Gauthier, F.; Ebert, B.; Taubert, R. D. et al. State-of-the art comparability of corrected emission spectra. 2. Field laboratory assessment of calibration performance using spectral fluorescence standards. *Anal. Chem.* **2012**, *84*, 3899–3907.

[62] Würth, C.; Grabolle, M.; Pauli, J.; Spieles, M.; Resch-Genger, U. Relative and absolute determination of fluorescence quantum yields of transparent samples. *Nat. Protoc.* **2013**, *8*, 1535–1550.